Astronomy & Astrophysics manuscript no.
(will be inserted by hand later)

HD 152248: evidence for a colliding wind interaction. ⋆

H. Sana, G. Rauw⋆⋆ †, and E. Gosset⋆⋆⋆ †

Institut d'Astrophysique et de Géophysique, Université de Liège, 5, Avenue de Cointe, B-4000 Liège, Belgium

Received December 2000 / Accepted date

Abstract. We present the results of a four year spectroscopic campaign on the early-type binary system HD 152248. Our analysis yields a new classification as O7.5III(f) + O7III(f) in contradiction with previous classifications of the components as supergiants. We derive improved orbital elements and the corresponding masses ($M_1 = 29.6\,M_\odot$ and $M_2 = 29.9\,M_\odot$) are somewhat larger than previously reported in the literature, though they are still significantly lower than the ones expected from evolutionary tracks. Both components of the system are rather close to fill their Roche lobe at periastron passage. We also investigate the equivalent width variations of the lines of the two components and we discuss their relation to the *Struve-Sahade* effect. Finally, we show that the line profile variability of the He II λ4686 and H α lines is consistent with a strong wind interaction between the two stars very much as predicted by current colliding wind models.

Key words. binaries: close – binaries: spectroscopic – Stars: early-type – Stars: fundamental parameters – Stars individual: HD 152248 – Stars: winds, outflows

1. Introduction

Early-type stars of spectral-type O or Wolf-Rayet (WR) undergo a considerable mass loss through their powerful winds. Within a binary system, we expect that the winds from both stars collide, forming a wind interaction region that can manifest itself through an enhanced X-ray emission. This X-ray emission from the shock can display a phase-locked modulation due to the variation of the line-of-sight opacity or due to a changing separation between the stars in eccentric binaries (Pittard & Stevens 1997). The wind-wind collision can also contribute to the formation of optical emission lines through the recombination process (e.g. Thaller 1997).
Over the last twenty years, the interest for wind interaction has grown, and numerous studies both from theoretical (e.g. Stevens, Blondin & Pollock 1992; Walder 1998; Pittard 2000) and observational (e.g. Corcoran 1996; Rauw, Vreux & Bohannan 1999; Hill et al. 2000) points of view have been undertaken. These studies demonstrate that considerable insight into the mass loss process can be gained from a detailed investigation of the wind interaction phenomenon. In addition, binary systems provide precious astrophysical laboratories allowing a direct determination of the fundamental parameters of the stars that are crucial to test evolutionary models and to probe the impact of binarity on the evolution of the components of the system.

HD 152248 is an O+O binary system that belongs to the young open cluster NGC 6231 which is considered as the nucleus of the rich Sco OB1 association. Situated at a distance of 1.99kpc (Baume et al. 1999), this cluster contains a number of interesting single O stars as well as O binaries and a WR+O system (WR79). Not only is the HD 152248 system one of the brightest objects of the cluster ($V = 6.06$, Baume et al. 1999) but it also appears from ROSAT X-ray observations to be the brightest X-ray source in NGC 6231. Corcoran (1996) has further shown that the ROSAT X-ray flux from HD 152248 displays phase-locked variations, though the poor phase coverage of the ROSAT data did not allow to elucidate their origin. On these grounds, NGC 6231 has been selected as a target for the XMM X-ray observatory as part of the Liège project for guaranteed time. The pointings will be centered on HD 152248 for a total duration of 180ksec, consisting of six 30ksec exposures in order to adequately sample the orbital variations.

In this context, we have undertaken a spectroscopic campaign to monitor the optical counterpart of most of the ROSAT X-ray sources of the NGC 6231 cluster. Some preliminary results have already been presented by Sana et al. (2001). The present paper is the first one of a series devoted to the O

Send offprint requests to: Sana, e-mail: `sana@astro.ulg.ac.be`

⋆ Based on data collected at the European Southern Observatory (La Silla, Chile) and at the Cerro Tololo Inter-American Observatory (Cerro Tololo, Chile).

⋆⋆ Chargé de Recherches FNRS (Belgium)

⋆⋆⋆ Chercheur Qualifié FNRS (Belgium)

† Visiting Astronomer, CTIO, National Optical Astronomy Observatories (NOAO). NOAO is operated by the Association of Universities for Research in Astronomy, Inc. under contract with the National Science Foundation.

stars in NGC 6231. We present here a complete and detailed spectroscopic study of the HD 152248 system (the main target of our campaign) in the optical domain. One aim is to derive accurate, contemporaneous ephemerides required to correctly interpret the forthcoming XMM data and to clarify the evolutionary status of both components of the system. Another objective of this study is the search for the optical signature of a wind interaction which is suspected to exist within the system because of its high and variable X-ray luminosity.

This paper is organised as follows. The next section is devoted to a review of the main results already published about this object in the literature. In the third section, we describe our spectroscopic observing campaign, the data we collected and the data reduction techniques we applied. The determination of the orbital parameters is presented in the fourth section. The fifth one is devoted to the study of the variations of the equivalent widths of the absorption lines and their link to the Struve-Sahade effect (S-S effect). We next turn to the emission lines displayed by the spectrum of this system. A particular attention is paid to the He II λ4686 and H α lines and to their phase-locked variability. Section 7 is devoted to the discussion of the evolutionary status of the system, and, among other things, we re-investigate its spectral and luminosity classification. Finally, we present a wind-wind interaction model that is consistent with most of the observational features of the emission lines. The last section is devoted to a brief summary of our main results.

2. Overview

HD 152248 is a double line O+O spectroscopic binary with a period close to six days. It was first reported to be a binary by Struve (1944), although he suggested an orbital period of 3 days. Walborn (1972) quoted a spectral type of O7.5I(n)(f)p for the composite spectrum. Hill et al. (1974, HCB hereafter) managed to separate the primary and secondary components and derived a period of 5.97days, assuming a zero eccentricity. Levato & Morrell (1983) confirmed the 6 day period and derived a non zero eccentricity ($e = 0.18 \pm 0.02$) for the system. A polarimetric study by Luna (1988) constrained the inclination of the orbit between 60° and 76°, with a preferred value of 71°. The study of the light curve of HD 152248 by Mayer et al. (1992) revealed that the system is displaying two eclipses of unequal depth and that both minima are not separated by 0.5 cycle, suggesting a non zero eccentricity. Based on IUE observations and using a cross-correlation technique, Stickland et al. (1996, ST96 hereafter) derived a period of 5.816083 days, an eccentricity of 0.124 and a mass ratio of 0.941. The deepest eclipse corresponds to the occultation of the less massive component. In order to avoid confusion we choose to adopt the ST96's convention for primary and secondary. In the following, we will thus refer to the component occulted during the deepest (i.e. primary) eclipse as the primary star of the system.

Based on the same set of IUE data and using a tomographic reconstruction algorithm to separate primary and secondary spectra, Penny et al. (1999, PGB hereafter) derived a spectral type of O7I+O7I. They also re-analysed the light curve of the system, complementing the Mayer et al. (1992) data set with Hipparcos observations. PGB showed that the system is displaying ellipsoidal light variations due to tidal deformations. They derived an inclination of 72° ± 3° for the orbit of the system and polar radii of $R_1 = 13.4 \pm 2.0\,\mathrm{R}_\odot$ and $R_2 = 12.9 \pm 2.0\,\mathrm{R}_\odot$ for the primary and secondary respectively. Combining spectroscopic and photometric results, they computed masses of $M_1 = 24.2 \pm 2.0\,\mathrm{M}_\odot$ and $M_2 = 25.8 \pm 2.0\,\mathrm{M}_\odot$. Howarth et al. (1997) reported that HD 152248 is displaying the *Struve-Sahade* effect, i.e. that the secondary lines seem to be stronger when the secondary is approaching. However, this result was not confirmed by PGB, who found no evidence for this effect in the strength of the cross-correlation function of the IUE spectra of HD 152248 with their standard star, HD 34078.

3. Observations and Data Reduction

3.1. Observations

We have been monitoring the HD152248 binary for four years (from May 1996 until May 2000), collecting a number of spectra with various instruments at the European Southern Observatory (ESO) and at the Cerro Tololo Inter-American Observatory (CTIO). In this section, we present the general features of the instrumental configuration and data reduction. The campaign we have undertaken represents a total of 69 useful spectra obtained during 49 nights spread over nine separate runs. The main journal of the observations is given in Table 1.

During two runs in May 1996 and March 1997, a set of medium resolution spectra has been obtained with the Boller & Chivens spectrograph (B&C) fed by the ESO 1.5m telescope. The detector was a 2k × 2k UV flooded Loral-Lesser CCD. The pixel size is 15 × 15μm. We used the holographic grating (ESO grating #32) with 2400 lines/mm, providing a spectral resolution of 1.2Å as measured from the FWHM of the lines of the HeAr comparison spectrum. The covered spectral range extends from λ3790 to λ4765Å.
High resolution spectra of the He I λ4471, N III $\lambda\lambda$4634-4641 and He II λ4686 lines were obtained with ESO's 1.4 m Coudé Auxiliary Telescope (CAT) at La Silla, using the Coudé Echelle Spectrometer (CES) equipped with the Long Camera (LC, before March 1998) or the Very Long Camera (VLC, after March 1998). The detector used was ESO CCD#38, a Loral 2688 × 512 pixel CCD with a pixel size of 15 × 15 μm. The slit width was chosen to achieve a nominal resolving power of 70000-80000. The effective resolving power as derived from the FWHM of the lines of the ThAr calibration exposures is 65000-75000. Typical exposure times were of the order of 20 minutes and the average S/N ratio is above 150. The wavelength domain is centered on the He I λ4471, N III λ4641 or He II λ4686 lines and is $\sim$ 40 Å and $\sim$ 20 Å wide for

Table 1. Main journal of the spectroscopic observations of the HD 152248 system. The first column lists the heliocentric Julian date (HJD). The second gives the observational phase as computed from our He I λ4471 RV orbital solution (cf. Table 3). Columns 3 and 4 (resp. 5 and 6) provide the He I λ4471 line RV (resp. the mean RV) for the primary and secondary stars, in the 'zero systemic velocity' reference frame (cf. text). The number of lines used to compute the mean RV is given in column 7 and the last column provides information about the instrumentation used.

HJD	ϕ	He I $\lambda\,4471-\overline{\gamma_{4471}}$		$\overline{RV_\lambda - \overline{\gamma_\lambda}}$		n	Instrument.
$-2\,450\,000$		RV_1	RV_2	RV_1	RV_2		
205.859	0.851	207.4	−208.0	212.7	−214.0	6	ESO1.5m+B&C
206.852	0.022	−11.6	−11.6	−56.3	38.1	6	ESO1.5m+B&C
207.816	0.188	−207.2	203.6	−200.8	204.2	6	ESO1.5m+B&C
208.795	0.356	−156.1	155.8	−166.8	164.4	6	ESO1.5m+B&C
208.879	0.370	−150.4	136.7	−148.9	164.1	6	ESO1.5m+B&C
209.789	0.527	−7.5	−7.5	1.7	1.7	6	ESO1.5m+B&C
209.903	0.546	−7.0	−7.0	−10.4	−8.6	6	ESO1.5m+B&C
210.782	0.698	167.3	−173.9	184.7	−167.2	6	ESO1.5m+B&C
210.910	0.720	187.2	−196.4	183.8	−199.2	6	ESO1.5m+B&C
211.777	0.869	186.7	−187.8	203.2	−180.6	6	ESO1.5m+B&C
211.912	0.892	175.0	−177.9	194.8	−178.9	6	ESO1.5m+B&C
534.902	0.426	−75.7	129.5	−110.3	95.9	6	ESO1.5m+B&C
535.904	0.599	70.7	−110.5	91.1	−114.9	6	ESO1.5m+B&C
536.888	0.768	213.2	−208.9	209.1	−210.1	6	ESO1.5m+B&C
537.897	0.941	98.7	−73.8	116.9	−121.8	6	ESO1.5m+B&C
538.889	0.112	−165.6	135.6	−163.5	156.3	6	ESO1.5m+B&C
539.907	0.287	−201.4	191.8	−200.0	191.5	6	ESO1.5m+B&C
531.908	0.912	160.2	−155.2	160.2	−155.2	1	CAT+CES+LC
532.881	0.079	−97.9	122.7	−97.9	122.7	1	CAT+CES+LC
533.859	0.247	−206.7	219.7	−206.7	219.7	1	CAT+CES+LC
534.844	0.416	−99.7	108.2	−99.7	108.2	1	CAT+CES+LC
535.859	0.591	48.7	−85.6	48.7	−85.6	1	CAT+CES+LC
536.856	0.762	219.0	−201.2	219.0	−201.2	1	CAT+CES+LC
622.604	0.506	−4.9	1.9	−4.9	1.9	1	CAT+CES+LC
623.628	0.682	154.2	−170.8	154.2	−170.8	1	CAT+CES+LC
624.554	0.841	215.8	−211.1	215.8	−211.1	1	CAT+CES+LC
625.607	0.022	−2.2	−2.2	−2.2	−2.2	1	CAT+CES+LC
626.571	0.188	−202.0	214.9	−202.0	214.9	1	CAT+CES+LC
1000.668	0.509	0.3	3.1	0.3	3.1	1	CAT+CES+VLC
1299.817	0.945	136.7	−91.8	130.4	−103.7	11	ESO 1.5m + FEROS
1300.809	0.115	−147.8	163.4	−150.5	166.8	11	ESO 1.5m + FEROS
1301.815	0.288	−204.3	202.5	−202.4	194.7	11	ESO 1.5m + FEROS
1302.808	0.459	−12.9	−12.9	−50.1	42.6	11	ESO 1.5m + FEROS
1304.889	0.817	223.2	−213.0	213.0	−210.3	11	ESO 1.5m + FEROS
1323.740	0.058	−88.6	49.4	−86.8	76.5	11	ESO 1.5m + FEROS
1327.780	0.753	199.2	−202.4	200.7	−202.9	11	ESO 1.5m + FEROS
1328.734	0.917	151.8	−150.2	158.2	−144.5	6	CTIO 1.5m + BME
1329.738	0.089	−130.2	117.9	−122.6	136.2	6	CTIO 1.5m + BME
1330.739	0.261	−215.9	194.0	−212.9	184.1	6	CTIO 1.5m + BME
1331.771	0.439	−81.4	36.7	−91.5	60.6	6	CTIO 1.5m + BME
1332.798	0.615	84.8	−108.4	94.7	−107.2	6	CTIO 1.5m + BME
1668.832	0.393	−108.1	131.5	−120.5	125.2	11	ESO 1.5m + FEROS
1669.853	0.568	36.0	−42.3	37.2	−51.4	11	ESO 1.5m + FEROS
1670.836	0.737	206.7	−190.0	204.2	−188.4	11	ESO 1.5m + FEROS
1671.839	0.910	157.9	−158.6	163.2	−159.3	11	ESO 1.5m + FEROS
1672.828	0.080	−122.7	102.1	−120.9	111.4	11	ESO 1.5m + FEROS
1673.809	0.248	−203.6	217.2	−206.4	207.6	11	ESO 1.5m + FEROS

spectra taken with the LC and the VLC respectively.

During three observing runs in April – May 1999, end of May 1999 and May 2000, a set of echelle spectra was taken with the Fiber-fed Extended Range Optical Spectrograph (FEROS) attached to the ESO 1.5 m telescope at La Silla. Thirty seven orders corresponding to a wavelength domain from 3650 to 9200 Å were observed. Typical exposure times were of the order of 6 minutes and the average S/N ratio is about 100, 220 and 150 at 4050, 6000 and 7500 Å respectively. The spectral resolving power of the FEROS instrument is 48000.

The detector was an EEV CCD with 2048×4096 pixels of $15 \times 15\,\mu$m.
Finally, another set of echelle spectra over the range 3850 to 5790 Å was obtained with the Bench-Mounted Echelle Spectrograph (BME) attached to the 1.5 m CTIO Ritchey-Chrétien Telescope, during a 5 night run in June 1999. Forty nine orders were observed using the KPGL2 316 lines mm^{-1} grating as a cross-disperser. The detector was a Tek 2048 CCD with $24\,\mu$m pixels. The slit width was set to $70\,\mu$m corresponding to a resolving power of 45000. Exposure times were of the order of 45 minutes and the average S/N ratio in the continuum is about 100.

3.2. Data reduction

The B&C and CAT observations were reduced in a standard way using the MIDAS package provided by ESO. Whenever possible, the spectra were rectified using a reference star observed under the same conditions. When such a spectrum was not available the spectra were normalized by fitting a polynomial to the continuum.
We used the FEROS context working under the MIDAS environment to reduce the FEROS echelle spectra. The reduction was performed using the *standard* option. Most of the unavoidable strong fringes that affect the red part of the spectrum (above 6600 Å) are simply corrected by flat-fielding. There are however a few residual fringes near 6670, 7140, 7385 and 7930 Å. Finally, the spectra were normalized over a range of a few hundred Å at once by fitting a polynomial of degree 4 or 5 to the continuum. Whenever doubt subsisted about the quality of the automatic merging between the different orders, we checked our results using the unmerged spectrum. Good agreement between both methods was generally observed.
The BME data were reduced using the IRAF[1] package and following the recommendations of the BME User's Manual. The pixel to pixel variations were removed using flat field exposures taken with a very bright light source and a diffusing screen placed inside the spectrograph (so-called *milky flats*). A first rectifying of the extracted echelle orders was carried out with the projector flat exposures. The spectra were then normalized by fitting a low-order polynomial to the continuum.

4. RV measurements and orbital solutions

The inspection of our data reveals that the spectra of the primary and secondary are very similar and that every absorption line detected is present in both spectra. Several lines are further present in emission and we will discuss them later in this paper.

4.1. RV measurements

We selected eleven pure absorption lines in the spectrum of HD 152248 to compute the orbital elements of the system. These lines were chosen according to the following criteria: the intensity of the line, the fact that they do not suffer a heavy blend with another neighbouring line at large RV separation phases (e.g. H δ, C IV $\lambda\lambda$5801-12) and the requirement that they should be free from pollution by any ISM lines (e.g. H ϵ) or telluric lines (e.g. He I λ7065). The selected lines are listed in Table 2. We measured the Doppler shifts by fitting two gaussians at phases where the separation between the lines of both stars was sufficient. We then used the cross-correlation like method described in Rauw et al. (2000) to attempt to disentangle the blended lines. As HD 152248 is an eclipsing binary, we used the light curve of PGB to achieve a rough first order correction of the relative line intensity at eclipsing phases. The observed lines are further affected by slight intensity and/or profile variations; we assumed, from our experience, that the errors on Doppler shifts measured in this way are about 2.5 times larger than the errors on the two-gaussian fit results. For those phases where the lines were too heavily blended for the latter method to give reliable results, we adopted the RV obtained with a single gaussian fit. We estimated, from the FWHM of the blend, that the accuracy on the line position in this latter case could be ten times lower than the one reached at large separation phases (i.e. with the two-gaussian fit method). While computing the orbital solution, we thus attributed a relative weight of 1.0, 0.15 and 0.01 to the RVs respectively measured with the two-gaussian fit, the cross-correlation like and the single gaussian fit methods. Ruling out the single gaussian fit points provides orbital parameters that are only marginally different.

We adopted the effective wavelengths for O stars listed in Table 2 to compute the barycentric RVs. These effective wavelengths are from Conti et al. (1977) below 5000Å, and from Underhill (1994) above. As our spectra taken with different instruments cover different wavelength ranges, the number of RV points associated with the different lines is variable. We report this number in column 6 of Table 2. The He I λ4471 line provides the largest data set with 47 RV points. These measurements are listed in Table 1.

4.2. Orbital solutions

4.2.1. The code

Our orbital solution computation code is based on a modified version of the Wolfe, Horak & Storer algorithm (see Wolfe et al. (1967) for the method; and Rauw et al. (2000) for the modifications implemented) and requires a previous knowledge of the orbital period to be run.

4.2.2. The period

The best (i.e. with the smallest r.m.s. error) estimate of the period from the literature is $P = 5.816083 \pm 0.000019$ days as given by ST96. As the He I λ4471 RVs are the most numerous among our RV data, we first used this set to investigate the period value. For this purpose we applied the Lafler &

[1] IRAF is distributed by the National Optical Astronomy Observatories.

Table 2. List of the absorption lines used to compute the orbital solution together with the adopted effective wavelengths. Column 3 gives the best-fit period value as deduced from the different RV data sets. The errors quoted were computed using the Wolfe, Horak & Storer algorithm. The primary and secondary *apparent* systemic velocities derived are respectively listed in columns 4 and 5. The last column provides the number of RV points associated with each line data set.

Line	Effective wavelength (Å)	Period (days)	$\gamma_{\lambda,1}$ (km s^{-1})	$\gamma_{\lambda,2}$ (km s^{-1})	n
He I λ 4026	4026.072	5.816072 ± 0.000196	-34.1 ± 3.7	-36.0 ± 8.1	30
He II λ 4200	4199.830	5.815943 ± 0.000187	-7.9 ± 3.1	-14.7 ± 6.4	35
H γ	4340.468	5.816123 ± 0.000222	-43.6 ± 3.9	-36.3 ± 8.8	35
He I λ 4471	4471.512	5.816045 ± 0.000092	-30.5 ± 1.5	-28.5 ± 4.3	47
He II λ 4542	4541.590	5.816022 ± 0.000116	-24.4 ± 2.0	-18.8 ± 4.9	35
He I λ 4713	4713.200	5.815972 ± 0.000224	-29.1 ± 4.3	-20.7 ± 9.6	30
H β	4861.190	5.816508 ± 0.000849	-37.2 ± 5.0	-37.7 ± 11.7	18
He I λ 4922	4921.929	5.815834 ± 0.000487	-26.8 ± 2.7	-23.5 ± 7.1	13
He I λ 5016	5015.680	5.816139 ± 0.000965	-19.9 ± 6.3	-12.6 ± 14.4	13
He II λ 5411	5411.520	5.815877 ± 0.000515	-19.0 ± 3.1	-15.3 ± 8.0	13
O III λ 5592	5592.370	5.816510 ± 0.000864	-18.8 ± 4.3	-22.2 ± 11.5	18

Kinman method (Lafler & Kinman 1965) and the generalized spectrogramme Fourier technique (Heck et al. 1985). The results obtained with both methods lie within 5×10^{-4} days of the value of ST96, which is one order of magnitude smaller than the error estimated from the width of the peak in the periodogramme. We then ran iteratively our code allowing for a differential correction of the orbital period. The convergence was reached in each case after a few iterations at most. This provides us with the period value which yields the orbital solution that best matches the observations (i.e. with the lowest r.m.s. residual) of the considered data set. Column 3 of Table 2 lists the period values obtained. Their weighted mean is $P = 5.816032 \pm 0.000058$ days, which is very close to the He I λ4471 value and contains both ST96 and Mayer et al. (1992) values within a $\pm 1\sigma$ interval. The very small uncertainty of the ST96 period determination results from the large time base of their IUE data set (∼5860 days) which is almost exactly four times ours. However, the HD 152248 system is most probably undergoing an apsidal motion of a few degrees per year (see below and Mayer et al. 2001) and the large time base of ST96 could actually bias their period determination. In the following, we choose to adopt our mean value $P = 5.816032$ days for the orbital period.

4.2.3. The orbital solutions

As a first step, we computed an orbital solution for each of the 11 absorption line data sets. Accounting for the error bars, the computed orbital elements do agree with each other, except for the *apparent* systemic velocities γ_1 and γ_2 (respectively associated with the primary and secondary star). Though the γ_1 and γ_2 values are in acceptable agreement with each other for the same line (see Table 2), their values as deduced from the different lines are indeed significantly different. This illustrates a well-known effect that different lines might reflect different systemic velocities. This might stem from the fact that these lines are formed at different depths in the atmosphere and thus at different outwards velocities, resulting in slightly different apparent systemic velocities.

In order to combine the RVs obtained from the different lines, we had to refer all the RV measurements to a "zero systemic velocity" reference frame. For this purpose, we simply subtracted the corresponding weighted mean between γ_1 and γ_2 from the individual RVs of the considered line. We then computed a weighted RV mean from all the RV data obtained at the same observing date. These mean RVs in the *zero systemic velocity* reference frame are listed in columns 5 and 6 of Table 1.

The computed orbital solutions from the He I λ4471 RV and the mean RV sets are both presented in Table 3. These two solutions are in excellent agreement with each other. Our way of combining the RVs from the different lines is further justified by the fact that the *apparent* systemic velocities computed from the mean data lie well within 1σ of the zero velocity. We also tested the value of the period found by ST96. This does not affect the r.m.s. residual by more than a few tenths of km s^{-1} and the difference between the computed orbital elements is not significant.

4.3. Physical parameters

The He I λ4471 velocity curve is plotted in Fig.1. This solution deduced from the optical wavelength domain is in good general agreement with the previous determination by ST96 from the UV domain. Our apparent systemic velocity is however 12 km s^{-1} more positive than theirs. This difference might result from the zero velocity point in their cross-correlation method, but it is probable too that the optical and the UV domains reflect different *apparent* systemic velocities. Though the primary parameters from both our and their solution are very close, a more intriguing discrepancy is the difference between the mass ratios deduced. Indeed our mass ratio (q=0.990) is much closer to unity than the ST96's one (q=0.941), and this manifests itself by the fact

Table 3. Computed orbital solution for HD 152248 using the RVs of the He I λ4471 absorption lines (left) or the mean RVs (right). T_0 is the time of the periastron passage.

	He I λ4471 common solution		Mean RVs common solution	
P(days)	5.816032 (fixed)			
e	0.127	$\pm$ 0.007	0.134	$\pm$ 0.006
$\omega(^o)$	84.8	$\pm$ 4.7	81.8	$\pm$ 4.3
T_0(HJD $-2\,450\,000$)	2003.879	$\pm$ 0.072	2003.841	$\pm$ 0.066
γ_1 (km s^{-1})	-30.3	$\pm$ 1.5	0.2	$\pm$ 1.4
K_1 (km s^{-1})	216.0	$\pm$ 1.5	216.6	$\pm$ 1.3
$a_1 \sin i$ (R$_\odot$)	24.59	$\pm$ 0.17	24.66	$\pm$ 0.15
γ_2 (km s^{-1})	-28.7	$\pm$ 4.3	2.6	$\pm$ 3.4
K_2 (km s^{-1})	213.7	$\pm$ 5.2	214.3	$\pm$ 4.2
$a_2 \sin i$ (R$_\odot$)	24.35	$\pm$ 0.62	24.40	$\pm$ 0.50
r.m.s. residual (km s^{-1})	9.5		8.2	
q $(= m_1/m_2)$	0.990	$\pm$ 0.023	0.990	$\pm$ 0.018
$m_1 \sin^3 i$ (M$_\odot$)	23.19	$\pm$ 1.2	23.34	$\pm$ 0.96
$m_2 \sin^3 i$ (M$_\odot$)	23.44	$\pm$ 0.73	23.58	$\pm$ 0.61

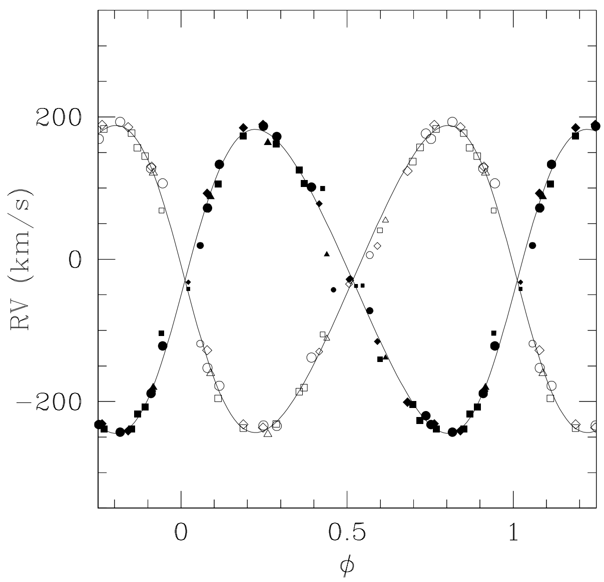

Fig. 1. Radial velocity curve of the HD 152248 binary system as computed from the He I λ4471 line plotted against the phase (ϕ). Different symbols refer to different instruments: triangle=BME, square=B&C, diamond=CES, circle=FEROS. Different sizes indicate different weights assigned to the data points in the computation of the orbital solution. Open symbols stand for the primary, while filled symbols indicate the secondary's RVs.

that our secondary component parameters K_2 and $a_2 \sin i$ are larger. The minimal masses we derive are also larger than the values inferred by ST96 and PGB. Adopting the PGB value for the inclination $i = 72°$ yields absolute masses of $M_1 = 27.0\,\mathrm{M}_\odot$ and $M_2 = 27.2\,\mathrm{M}_\odot$ for the primary and the secondary respectively. We used Eggleton's formula (Eggleton 1983) to estimate the radii of the Roche lobe (RRL) for both components. Again assuming $i = 72°$ yields respectively $RRL_1 = 19.45\,\mathrm{R}_\odot$ and $RRL_2 = 19.55\,\mathrm{R}_\odot$ if we neglect the effect of the eccentricity (however see below). Thus if we adopt $R_1 = 13.4\,\mathrm{R}_\odot$ and $R_2 = 12.9\,\mathrm{R}_\odot$, this result confirms the assertion of PGB that the system should not be undergoing a Roche lobe overflow (RLOF) mass transfer. However, Mayer et al. (2001) reported a lower value for the inclination ($i = 67.2°$) and larger radii ($R_1 = 15.6\,\mathrm{R}_\odot$ and $R_2 = 17.1\,\mathrm{R}_\odot$). In this latter case, the primary and secondary are respectively filling 72 and 91% of their Roche lobe volume at periastron. If these preliminary results of Mayer et al. (2001) for the radii are confirmed, we then expect the system to be very unstable near periastron passage and important mass transfer or mass loss could be initiated.

4.4. Apsidal motion

While recomputing the orbital solution from previously published RV data at different epochs in order to check the consistency of our method, we were led to suspect the presence of an apsidal motion within the binary system HD 152248. In the following investigation, we considered three sets of data that are summarized in Table 4. We decided to ignore the complementary data obtained by HCB near JD$\sim$2 440 000 because their very poor phase coverage did not allow to derive any significant constraint on the longitude of periastron. Keeping the value of the orbital period and the eccentricity fixed at our new value, we have fitted the RV data from the literature. Table 4 lists the ω values that provide the best fit to the various data sets. From these results, it is clear that the system is undergoing an apsidal motion. A simple linear regression yields a rate for the apsidal motion of about 3.4° yr^{-1}. A more detailed study by Mayer et al. (2001) based on new recent photometric results is currently on the way. These authors independently discovered the presence of an apsidal motion in HD 152248 and they estimate a period of 132 years, in acceptable agreement with our value.

Table 4. Summary of the investigation we undertook to estimate the apsidal motion of the HD 152248 system. Second to fourth columns list respectively the approximative mean JD in format JD$-$2 400 000, the time interval (expressed in days) and the number of RV points in the set. Column 5 reports the values of the angle of periastron passage (ω) which provide the best fit. The last column lists the r.m.s. residual between the best fit and the data.

Data set	$\overline{JD}$	Time base	n	ω (°)	r.m.s. (km s^{-1})
Struve[1]	$\sim$31 200	14	22	-95	27.5
ST96	$\sim$48 500	5861	26	76	12.1
This work	$\sim$51 000	1468	47	85	9.2

1. Struve (1944); also described in HCB

5. Equivalent widths and S-S effect

Using a two-gaussian fit, we measured the EWs of the primary and secondary absorption lines listed in Table 2, except near conjunction. A particular attention has been paid to the normalization process to avoid systematic deviations. We estimate that our continuum determination is self-consistent with an accuracy better than 0.5%. For the strongest lines, this corresponds to a maximum contribution to the error on the EW measurements of about 0.05Å. We further estimate that the mean contribution of the continuum determination to the error is rather about 0.02Å and that the intrinsic error related to the measurement process is of the same order of magnitude.
Several clear tendencies appear from these measurements and are presented below. First of all, let us divide the orbital cycle into four parts which we call quadrants, each of them corresponding to an interval of 90° in true anomaly. The first quadrant ranges then from the primary eclipse to the first quadrature; the second, from the first quadrature to the secondary eclipse and so on for the third and fourth quadrants. Due to the blend near conjunction, the effective corresponding phase intervals are, respectively for 1st to 4th interval, [0.06-0.22], [0.22-0.40], [0.66-0.80] and [0.80-0.95]. To limit the uncertainties and outline the observed trends, we computed the mean EWs over each of the quadrants. These are listed in Table 5. The primary to secondary ratios of the mean EWs in each quadrant are further plotted in Figs. 3 and 4.

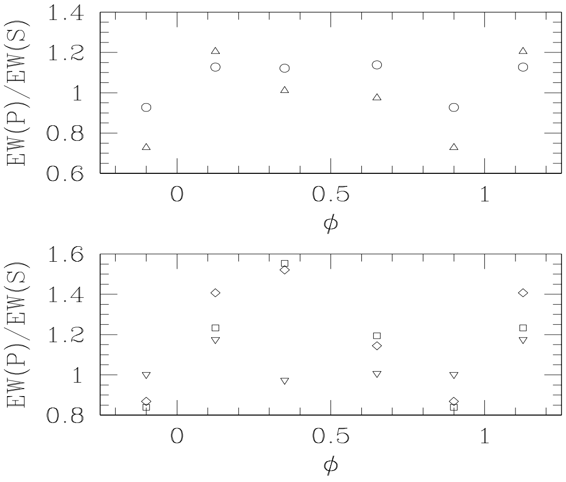

Fig. 3. Primary to secondary ratios of the mean EWs of the He I lines in each quadrant. Downwards triangles = He I λ4026, circles = He I λ4471, diamonds = He I λ4713, squares = He I λ4922, upright triangles = He I λ5016.

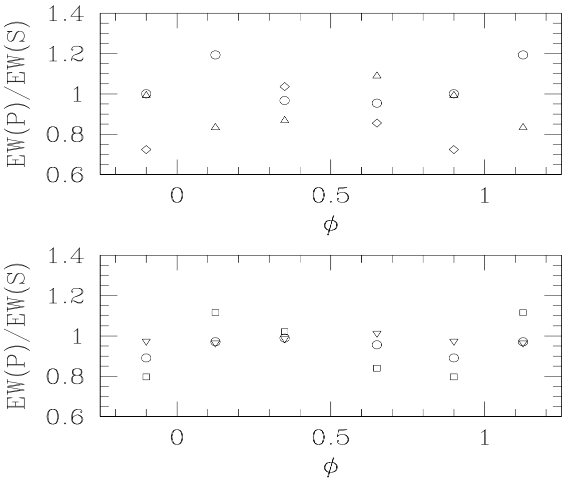

Fig. 4. Primary to secondary ratios of the mean EWs of the Balmer and the O III (upper panel) lines and of the He II (lower panel) lines in each quadrant. Upper panel: circles = Hγ, diamonds = Hβ, upright triangles = O III λ5592. Lower panel: squares = He II λ4200, circles = He II λ4542, downwards triangles = He II λ5411.

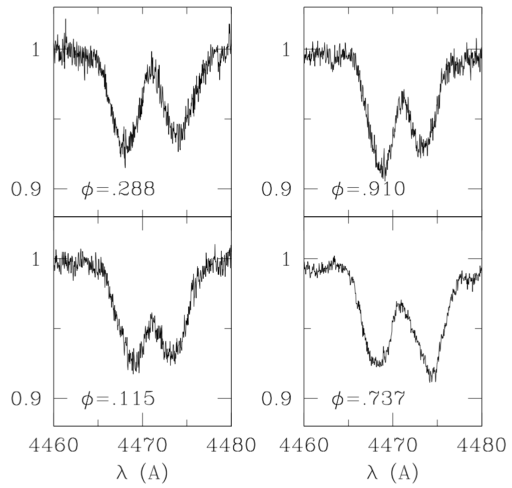

Fig. 2. Illustration of the variation of the He I λ4471 lines strength. Note that the primary is on the blue side of the spectra at phases ϕ = 0.115 and 0.288 while it is on the red side of the spectra at the phases shown in the right panel. The depletion in the red wing of the spectrum at ϕ = 0.737 is the blue shifted secondary Mg II λ4481 line.

From these figures, we can identify the following trends:

1. The He I lines: a very intriguing variation is observed for the He I λ4471 line and is also present in other He I lines. The primary to secondary EW ratio is reversed in the fourth quadrant. Indeed, during the first three quadrants, the lines associated with the primary are slightly more intense than the secondary ones. In the fourth quadrant (i.e. ϕ = 0.8-1.0) however the situation is exactly the opposite with the primary's lines being fainter. Thus the secondary lines seem stronger between phases 0.8 and 1.0, when the star is approaching. However, we have to mention that this effect is not detected for the He I λ4026 line, but this line is actually a blend with the He II λ4026 transition.
2. The He II lines: a clear enhancement of the secondary lines compared to the primary ones is observed for the He II

Table 5. List of the mean equivalent widths (expressed in Å) over each of the four quadrants (see text). The P and S letters stand for Primary and Secondary respectively.

Line	Quadrant 1		Quadrant 2		Quadrant 3		Quadrant 4	
	P	S	P	S	P	S	P	S
He I λ4026	0.281	0.239	0.242	0.248	0.258	0.256	0.265	0.264
He I λ4471	0.299	0.265	0.296	0.264	0.302	0.265	0.266	0.287
He I λ4713	0.095	0.068	0.094	0.062	0.086	0.075	0.063	0.073
He I λ4922	0.101	0.082	0.116	0.075	0.107	0.090	0.087	0.104
He I λ5016	0.106	0.088	0.097	0.096	0.098	0.101	0.083	0.114
He II λ4200	0.188	0.168	0.173	0.169	0.195	0.233	0.185	0 .232
He II λ4542	0.280	0.288	0.283	0.286	0.283	0.296	0.268	0.301
He II λ5411	0.421	0.436	0.425	0.431	0.439	0.433	0.418	0.429
H γ	0.914	0.766	0.804	0.832	0.812	0.851	0.837	0.836
H β	n.	n.	0.758	0.732	0.740	0.865	0.603	0.833
O III λ5592	0.195	0.234	0.260	0.299	0.203	0.186	0.191	0.193

$\lambda\lambda$4200 and 4542 lines during the 3rd and 4th quadrants, while the secondary is approaching. However the He II λ5411 line does not seem to display any significant variation of the EW ratio (Fig. 4).

3. The Balmer lines: these lines do not seem to display such a clear general trend as the He I or He II lines. Indeed, though the four Balmer absorptions (i.e. Hβ, Hγ, H δ and Hϵ) most often exhibit the blueshifted component with the largest EW, this probably results, for the H δ and H ϵ lines, from a blend with neighbouring lines on the blue side. The H γ line displays an inversion of the primary and secondary EW ratio between the 1st and 2nd quadrants. Finally though none of the H β spectra could be separated in the 1st quadrant, the secondary line is clearly strengthened when this star is approaching (i.e. quadrants 3 and 4). The primary line also seems fainter at those phases.
4. The O III λ5592 line: this line displays a behaviour opposite to the ones of the lines previously discussed. In this case, the secondary line is fainter in the 3rd and 4th quadrants, while the secondary star is approaching.

As suggested by Howarth et al. (1997), these variations might be related to the so-called Struve-Sahade effect (S-S effect) though the origin of this effect is still not fully understood. First reported by Struve (1937), the *Struve-Sahade effect is the apparent strengthening of the secondary spectrum of a hot binary when the secondary is approaching and the corresponding weakening of the lines when it is receding* (Bagnuolo et al. 1999). We refer to the paper of Bagnuolo et al. for a recent review of the problem. In their paper, Bagnuolo et al. re-analysed three systems previously reported to display this effect and concluded that these "*three classical massive binaries* [...] *have a different tale*": localized heating by colliding winds for AO Cas, no Struve-Sahade effect for Plaskett's Star and a probable RLOF scenario for 29 CMa. So the Struve-Sahade effect is thus probably a similar manifestation of different physical phenomena and must then be investigated one case at a time.

Strictly spoken, only H β and two of the three studied He II lines display the S-S effect. Indeed, the variation of the He I line intensity does not match the 'classical' definition of the S-S effect as the strengthening of the secondary lines and the corresponding weakening of the primary ones happen between the 3rd and the 4th quadrants. A detailed investigation of the intrinsic variations of the EWs related to each star would further require to correct them from the relative contribution of the primary and secondary fluxes to the continuum. However we have to defer this task to future works as we do not have at our disposal, at this stage, the appropriate photometric information required to properly carry out this study.

Finally, Gayley (2001) has recently suggested that the S-S effect might be due to surface flows generated by the irradiation of the stellar surface by the companion. This could modify the rotational broadening of the lines and might break down the approaching/receding symmetry, resulting in shallower or deeper absorption lines according to the line of sight. However no influence on the intensity of the line is expected due to surface flows. The maximum projected velocity of such surface flows predicted in the case of the components of HD 152248 lies near 110 km s^{-1}. The measured FWHMs of the absorption lines in the spectrum of HD 152248 present a scatter of about 0.3-0.4 Å around the mean value, though no clear correlation with the phase is observed. This corresponds to a variation of the broadening velocity of about 25 km s^{-1}. The exact contribution of surface flows induced by irradiation to these slight profile variations is unknown. Clearly, detailed numerical modelling as well as more observations combining very high S/N and high resolution are needed to clarify this question.

6. The emission lines

As mentioned earlier in this paper, the HD 152248 spectrum presents several emission features. These include the He II λ4686 and H α lines that consist of a mixture of absorption and emission lines, the heavily blended N III $\lambda\lambda$4634-4641 features, the C III λ5696 line and the faint unidentified Of emissions at λ4486 and λ4504.

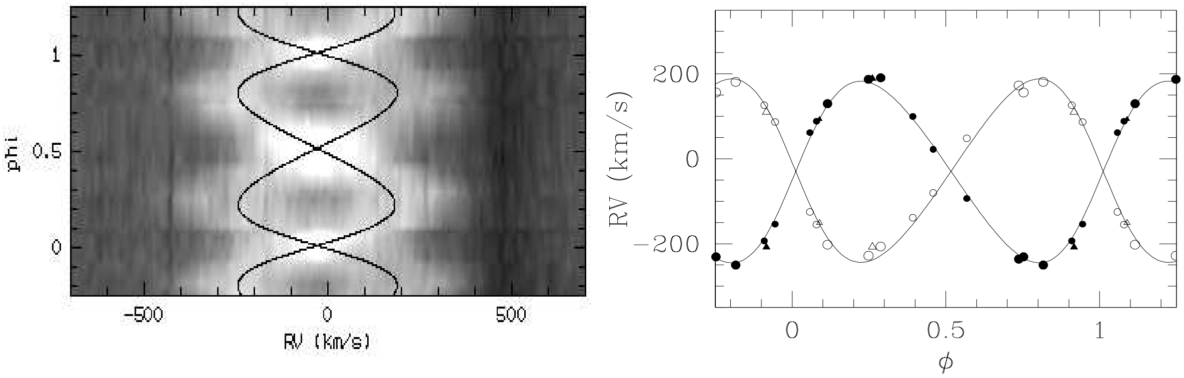

Fig. 5. Left: dynamical spectrum of the C III λ5696 emission line. The cuts are set to [0.97-1.08]. The He I λ4471 line RV curve has been overplotted. Right: RVs of the C III λ5696 line overplotted on the He I λ4471 line RV curve. The symbols used have the same signification as in Fig. 1.

6.1. The C III *λ5696 line*

As it clearly appears from Fig. 5, the C III λ5696 emission line turns out to be double peaked around quadrature and the peaks seem to move in phase with the RV curves of the absorption lines. In order to measure the RVs associated with these peaks, we first modelled the diffuse interstellar band (DIB) at λ=5704.97Å (EW≈0.064Å) on a spectrum where it was well separated from the C III line (HJD 2451669.853). We then subtracted the modelled DIB from all spectra and fitted two gaussians to the C III emission line whenever the separation between the components was large enough; at other phases, we used the cross-correlation like method. The measured RVs are plotted together with the He I λ4471 RV curve on the right panel of Fig. 5. The left panel presents a grey scale image around the C III line; the He I λ4471 line orbital solution has been overplotted. It is clear from the two panels of Fig. 5 that the C III λ5696 lines closely follow the orbital motion. As we already pointed out in the case of HD 93403 (Rauw et al. 2000), this is a strong argument in favour of a photospheric origin of the C III λ5696 line as suggested by Nussbaumer (1971) and Cardona-Núñez (1978). Finally, unlike the case of HD 93403 (see Rauw et al. 2001), the C III λ5696 line in the spectrum of HD 152248 does not seem to display a reversal of the intensity ratio due to the Struve-Sahade effect.

6.2. The N III *$\lambda\lambda$4634-4641 structure*

The HD 152248 spectrum presents a highly complex emission structure between about λ=4625Å and λ=4645Å, which displays important phase-locked profile variations. In this region of the spectrum, the N III $\lambda\lambda$4634 and 4641 lines are heavily blended with each other as well as with the neighbouring Si IV λ4631 and C III $\lambda\lambda$4647-4650 lines at all phases. Due to their lower resolution, we excluded the B&C spectra from our study. Similarly we did not consider the CTIO spectra because of their relatively lower S/N ratio. A complementary journal of the CAT N III $\lambda\lambda$4634-4641 observations is given in Table 6. A careful comparison of the CAT and FEROS N III $\lambda\lambda$4634-4641 spectra with the predicted line positions computed from our ephemerides and our orbital solution allows us to identify the components of the blend. Both stars of the HD 152248 system present the N III $\lambda\lambda$4634-4641 lines in emission in their spectra. Following e.g. Mathys (1988) an (f) tag should then be added to their spectral classification. The Si IV λ4631 and C III $\lambda\lambda$4647-4650 lines are in absorption in both spectra.

6.3. The unidentified $\lambda\lambda$4486, 4504 lines

The two $\lambda\lambda$4486, 4504 emission lines are related to the Of phenomenon and still remain unidentified though they have been known for several decades now. These two lines are rather faint in the spectra of HD 152248 and their peak intensities reach maxima of respectively 2.5% and 2% of the continuum level at conjunction phases. The stellar Mg II λ4481 lines, the DIB near λ4502 and the probable presence of the N III $\lambda\lambda$4510-4514 absorption lines render this region of the spectrum very crowded and prevent us from performing a detailed analysis. It seems however clear that the λ4486 line is double peaked with the two components closely following the orbital motion. The situation is less clear concerning the λ4504 line, because of the DIB that affects the blue side of the line. A careful inspection of the spectra however suggests that the λ4504 line might also be double peaked according to the orbital motion.

6.4. The He II *λ4686 and* H α *lines*

We have a total of 51 He II λ4686 line spectra (17 B&C, 16 CES, 5 BME and 13 FEROS) at our disposal that provide a very good phase coverage. The journal of the CAT observations of He II λ4686 is given in Table 6. Our H α line data set is much more limited and consists of only 13 FEROS spectra. The normalization of the FEROS spectra around these two lines turned out to be a rather difficult task. Indeed, both lines are situated at the junction of two echelle orders and we had to normalize the spectra locally. To compare the B&C

Table 6. Complementary journal of the CAT observations of the N III $\lambda\lambda$4634-4641 and He II λ4686 lines. The notations used are identical to those of Table 1.

Line	HJD −2 450 000	ϕ	Instrument.
N III $\lambda\lambda$4634-41	621.781	0.364	CAT+CES+LC
	622.802	0.540	CAT+CES+LC
	623.805	0.712	CAT+CES+LC
	624.771	0.878	CAT+CES+LC
	625.785	0.053	CAT+CES+LC
	626.762	0.220	CAT+CES+LC
He II λ4686	532.911	0.084	CAT+CES+LC
	533.902	0.254	CAT+CES+LC
	534.897	0.425	CAT+CES+LC
	535.895	0.597	CAT+CES+LC
	621.707	0.351	CAT+CES+LC
	622.735	0.528	CAT+CES+LC
	623.741	0.701	CAT+CES+LC
	624.700	0.866	CAT+CES+LC
	625.714	0.040	CAT+CES+LC
	626.696	0.209	CAT+CES+LC
	995.821	0.676	CAT+CES+VLC
	996.782	0.841	CAT+CES+VLC
	997.767	0.011	CAT+CES+VLC
	998.753	0.180	CAT+CES+VLC
	999.760	0.353	CAT+CES+VLC
	1000.727	0.520	CAT+CES+VLC

Table 7. Measured equivalent widths of the three components of the He II λ4686 and H α lines as measured on the spectrum taken on HJD 2451673.809 (ϕ=0.248).

Line component	EW(He II λ4686) (Å)	EW(H α) (Å)
Primary absorption	0.245	0.590
Secondary absorption	0.178	0.400
Emission	−0.630	−2.588

spectra with the echelle spectra, we also had to apply a local normalization around He II λ4686 on the B&C spectra, in order to account for the broad underlying emission extending from 4600 to 4720Å.

Both the He II λ4686 and H α lines consist of a mixture of absorptions and emissions. Dynamical spectra of these two lines are displayed as a function of orbital phase on the grey-scale images in Fig. 7. These were built by direct linear interpolation along the time axis of the observed spectra.
It is clear from these two diagrams and from Fig. 6 that the He II λ4686 and H α line profiles are strongly variable. For both lines, we can identify two absorption components at RVs that closely match the orbital motion. These absorptions are thus most probably formed in the atmosphere of the stars of the system. These two absorption features are superimposed on a broader emission component. The width of this latter emission varies with orbital phase (see e.g. Fig. 6).
To quantify these variations, we first measured the total EW

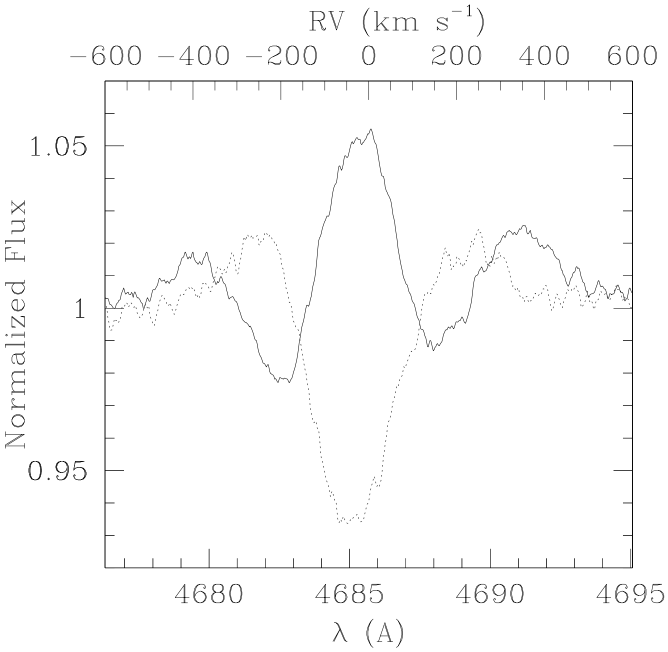

Fig. 6. Two superimposed spectra of the He II λ4686 line: the full line corresponds to $\phi = 0.910$; the dashed line, to $\phi = 0.568$.

of the lines. The results for both lines are plotted against the phase in Fig. 8. Concerning the He II λ4686 line, we notice that the absorption is clearly dominating near phase $\phi = 0.5$ and in a less prominent way near $\phi = 0.0$. On the other side, the emission is overwhelming at phase $\phi \approx 0.8$ (and to some extent at $\phi \approx 0.25$).

We next attempted to restore the emission component. To this aim, in order to model the three line components, we fitted three gaussians to the line profile on a spectrum where the two absorption contributions are well separated. The EWs of all three components as obtained from the fit are reported in Table 7. These results should however be considered with caution since the EWs of the three components are most probably undergoing some variation with phase. For each observed spectrum, we then shifted the template of the absorption components according to our He I λ4471 orbital solution and the observation phase, and we subtracted the shifted fake lines from the observed profile. This 'restoration' process is a very crude method. In fact, the apparent systemic velocities of the He II λ4686 and H α absorption components are unknown and could be different from that of the He I λ4471 line, though Fig. 7 suggests that this difference should be small. In addition, HD 152248 displays both ellipsoidal variations and photometric eclipses. As a consequence, the EWs of the lines are most probably varying with phase, and it is almost impossible to correctly account for this effect without the exact knowledge of the amount of light originating from the primary and from the secondary at each orbital phase. However, we used the eclipse depths from PGB to derive a first order correction for the line intensities of the absorbing components. We then measured the full width at the base of the restored emission components. To this aim, we defined the limits of the

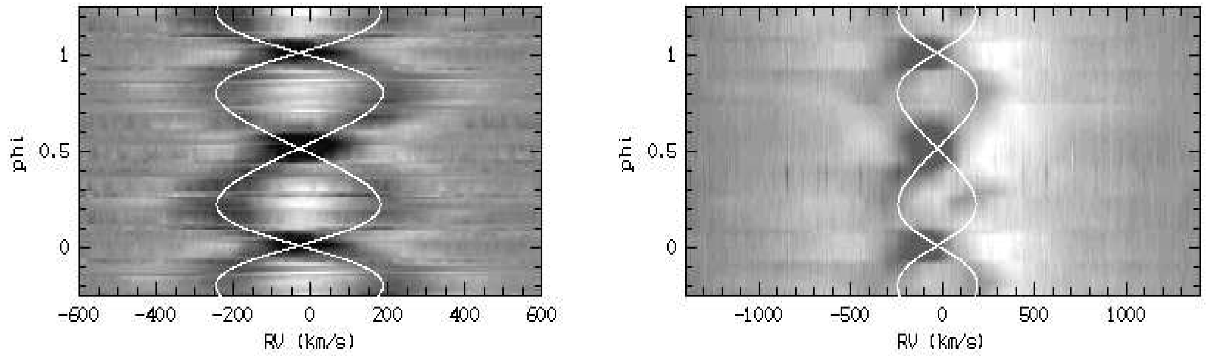

Fig. 7. Dynamical spectra of the He II λ4686 (left) and H α (right) lines. The cuts are respectively set to [0.95-1.05] and [0.95-1.1]. The He I λ4471 RV curve has been overplotted on both panels.

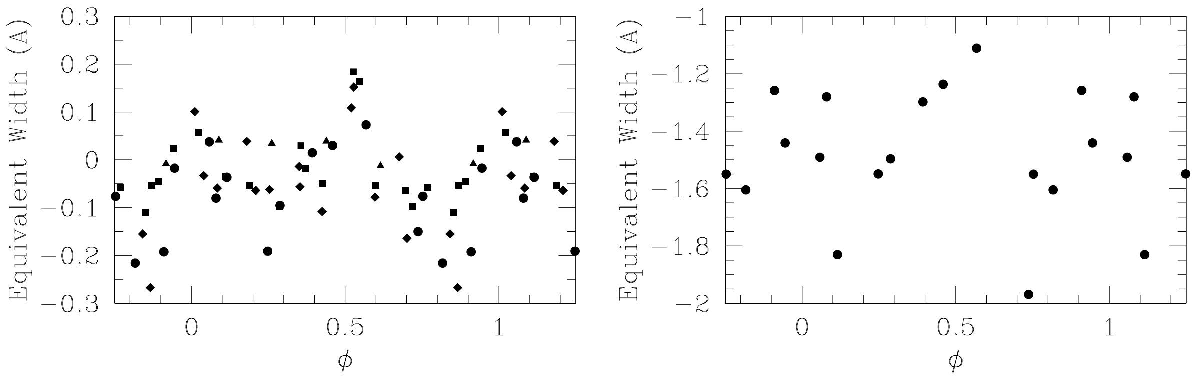

Fig. 8. Equivalent widths of the He II λ4686 (left) and H α (right) lines. Different symbols refer to different instruments: triangle=BME, square=B&C, diamond=CES, circle=FEROS.

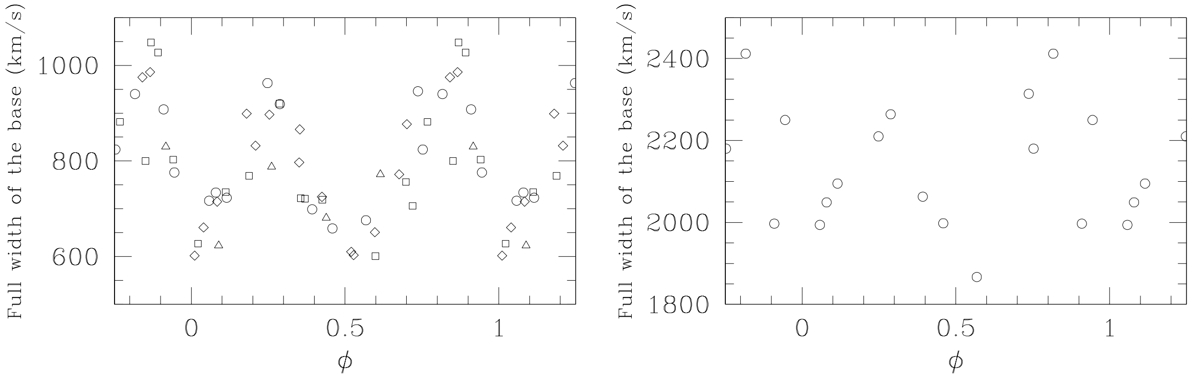

Fig. 9. Full widths of the base of the emission component of the He II λ4686 (left) and H α (right) lines. Different symbols refer to different instruments: triangle=BME, square=B&C, diamond=CES, circle=FEROS.

emission at a normalized intensity of 1.01, i.e. we considered the emission above 1% of the continuum. Results are displayed in Fig. 9 and show a strong phase-locked variation of the full width at the base of the emission components. Similar measurements have been carried out on the raw observed spectra to check that our restoration method does not bias the results. Only slight differences of the order of 20km s^{-1} for the start and end positions of the He II λ4686 emission component were detected. The H α emission component being much more intense, no significant difference could be detected for this line.

In summary, the He II λ4686 and H α lines behave similarly in many points. A common interpretation of the observed phase-locked modulation of both lines will be provided in Sect. 8, within the framework of a colliding wind model. However, we first need to discuss the evolutionary status of the components of HD 152248 .

7. Evolutionary status

7.1. Spectral type and luminosity classes

Following the criterion of Conti (1973), we use the logarithm of the EW ratio of He I $\lambda4471$ and He II $\lambda4542$ to determine the spectral types of both components of the system. We get for the mean ratio:

$$\log W'_{prim}(\lambda4471/\lambda4542) = 0.013\,[-0.035, 0.056]$$
$$\log W'_{sec}(\lambda4471/\lambda4542) = -0.044\,[-0.101, 0.006]$$

This gives a spectral type of O7.5 and O7 for the primary and secondary stars respectively. The values between brackets correspond to a 1σ dispersion on the mean value of the EW ratios. The agreement with the previous determination by PGB using IUE data (O7+O7) is quite good.

Walborn (1972) quoted a supergiant luminosity class for the composite spectrum of HD 152248 though he noted that his classification could be vitiated because of the peculiar He II $\lambda4686$ profile. PGB also adopted a supergiant luminosity class for both components of the system. However, the presence of He II $\lambda4686$ and H α in absorption in the spectrum of both stars argues against such a classification. In fact, PGB's assertion was based on the following UV criteria: a very strong emission in the Si IV $\lambda\lambda1394$-1403 lines in all the IUE composite spectra and a blue asymmetry and red emission in the N IV $\lambda1718$ line in both primary and secondary spectra. However, as these authors mentioned in Penny et al. (1996), the Si IV $\lambda\lambda1394$-1403 doublet is a *wind feature* that might not be associated with the photosphere. Furthermore, the dependence of the N IV $\lambda1718$ line on wind strength might lead to a more luminous classification in the case of a star with an unusually strong wind. We believe that previous confusion about the luminosity class of this system arises mainly from the fact that the lines adopted as luminosity classification criteria are probably affected by a wind interaction process occurring within the HD 152248 system (see below).
Based on the presence of He II $\lambda4686$ and H α in absorption in the spectrum of both components, we follow Mathys (1988) recommendation and, according to a rough determination of the EW of the He II $\lambda4686$ absorption components (from Table 7), we adopt a giant luminosity class for both stars of the HD 152248 system. Morrell et al. (1991) further showed that the unidentified $\lambda\lambda4486$, 4504 lines display a clear luminosity dependence. An estimate of the intensity of the $\lambda4486$ line in the spectrum of HD 152248 also suggests that the stars of HD 152248 are giants.

Finally both stars present N III $\lambda\lambda4634$-4641 in emission so that, associated with weak He II $\lambda4686$ absorption, an (f) tag should be added to the spectral classification. The new classification for this system is thus: O7.5III(f) + O7III(f).

7.2. Location in the H-R diagram

Adopting the effective temperature calibration of Chlebowski & Garmany (1991), the spectral types derived above yield $T_{\rm eff} = 37100 \pm 1000$ K and $T_{\rm eff} = 38100 \pm 1000$ K for the primary and the secondary respectively. The quoted uncertainty corresponds to half a spectral subtype.

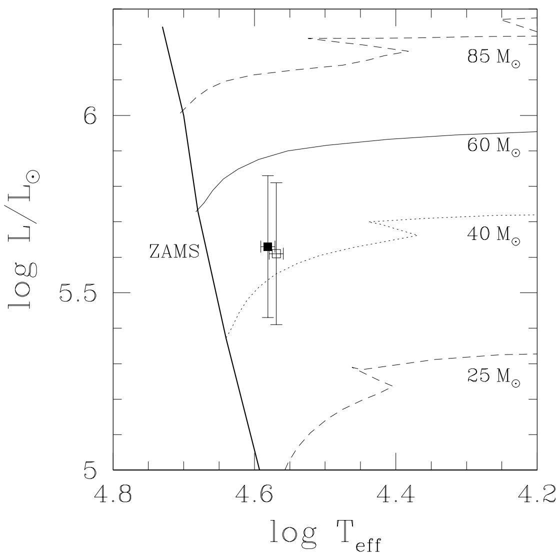

Fig. 10. Hertzsprung-Russell diagram of the HD 152248 system. The open and filled symbols stand for the primary and secondary respectively. Evolutionary tracks are from Schaller et al. (1992) for Z=0.020 and adopting 'standard' mass loss rates.

Howarth et al. (1997) and Penny et al. (1999) quote a luminosity ratio in the UV and in the visible of $I_{\rm sec}/I_{\rm prim} \simeq 0.98$. Raboud, Cramer & Bernasconi (1997) reported $V = 6.09$ and $E(B-V) = 0.46$ for HD 152248. The photometry of HD 152248 is affected by the presence of a nearby visual companion that is about 2.0 magnitudes fainter than the close binary (Mason et al. 1998). The values of the distance modulus of the NGC 6231 cluster range from 10.7 to 11.6. In the following, we will adopt the value $DM = 11.2$ derived by Raboud et al. (1997). We thus obtain $\log(L_{\rm bol}^{\rm prim}/L_\odot) = 5.61 \pm 0.2$ and $\log(L_{\rm bol}^{\rm sec}/L_\odot) = 5.63 \pm 0.2$ for the primary and secondary respectively. The uncertainties on the quoted luminosities correspond to the sole uncertainty (0.5 dex) on the distance modulus of NGC 6231.

The locations of the components of HD 152248 are plotted in a H-R diagram in Fig. 10 together with the evolutionary tracks of Schaller et al. (1992). From the above results, we can infer radii of $R_1 = 15.4^{+3.9}_{-3.1}\,{\rm R}_\odot$ and $R_2 = 14.9^{+3.9}_{-3.1}\,{\rm R}_\odot$. These radii overlap within the errors with the values derived by PGB (13.4 and 12.9 R$_\odot$ for the primary and secondary respectively) and Mayer et al. (15.6 and 17.1 R$_\odot$ for the primary and secondary respectively). Our values of the radii are slightly larger than the typical radii of O7 - O7.5 giants as listed by Howarth & Prinja (1989), but they are definitely smaller than the radii of luminosity class I stars of same spectral type (Howarth & Prinja 1989) lending further support to our assertion that the components in HD 152248 are giants rather than supergiants.
From a crude interpolation between the evolutionary tracks

of Schaller et al. (1992), we derive 'theoretical' masses of $M_1 = 41.7^{+10.3}_{-6.1}\,\mathrm{M}_\odot$ and $M_2 = 43.7^{+10.1}_{-6.1}\,\mathrm{M}_\odot$. If we adopt the inclination of 67.2° as determined by Mayer et al. (2001), the minimal masses reported in Table 3 yield observed masses of 29.6 and 29.9 $\mathrm{M}_\odot$ for the primary and the secondary respectively. These latter values are significantly smaller than the masses predicted from the theoretical models for stars at the same location in the HR diagram. This problem was already pointed out by PGB. Improved stellar evolution models including the effects of rotation (Meynet & Maeder 2000) might provide a solution for this mass discrepancy. In fact, the new models discussed by Meynet & Maeder (2000) predict a large scatter in the mass-luminosity relation that can amount to a difference of 30% in mass. However, we caution that the components of HD 152248 do not show an exceptionally large projected equatorial rotational velocity (see Howarth et al. 1997).

Another way to account for this mass discrepancy consists to postulate a Roche lobe overflow scenario that could have altered the evolution of the components. Indeed the stars are close to their stability limit near periastron passage and mass loss could be initiated at that time. However, we did not find any evidence that such a process is currently on the way in HD 152248. The stars might however have been transferring mass through the L_1 point in the past, though the amount of transferred mass as well as the reason why this process came to a stop are unclear. Finally, we also mention Gayley's suggestion (Gayley 2001) that non-conservative mass transfer prior to the RLOF phase might exist in highly eccentric close binaries. As this is still a 'working idea', we refer to his paper for more details.

8. Wind-wind interaction

It is now time for the difficult task of consistently explaining all our observations. It is obvious, from the results presented above, that both components of the HD 152248 system are very similar. They indeed have similar polar radii, masses, luminosities and spectral types. Therefore, we can expect that the stars also have similar wind properties (mass loss rates and asymptotic velocities). Howarth et al. (1997) derived terminal velocities of $v_{\infty,1} = 2420\,\mathrm{km\,s^{-1}}$ and $v_{\infty,2} = 2010\,\mathrm{km\,s^{-1}}$ for the primary and secondary respectively. We can use the stellar parameters derived above in conjunction with the theoretical mass loss recipe of Vink et al. (2000) to estimate the mass-loss rates of the two components. In this way, we obtain $\log \dot{M}_1 = -5.53$ and $\log \dot{M}_2 = -5.48$ ($\mathrm{M}_\odot\,\mathrm{yr}^{-1}$) yielding a wind momentum ratio (Stevens et al. 1992) of

$$\mathcal{R} = \left(\frac{\dot{M}_1\, v_{\infty,1}}{\dot{M}_2\, v_{\infty,2}}\right)^{1/2} \simeq 1.03$$

From these simple arguments, we expect therefore that the stagnation point of a wind-wind collision should be located near the center of mass of the HD 152248 system. Adopting a 'standard' β velocity law (with $\beta = 1$), we find that, depending on the orbital separation, the winds of both stars should reach between about 0.34 and $0.50 \times v_\infty$ before they collide. Using these pre-shock velocities, we obtain rather low values of the cooling parameter $\chi \leq 0.02 - 0.15$ (see Stevens et al. 1992 for the definition of χ). Radiative cooling could therefore play an important role in the interaction region and cool the shock-heated material to temperatures where the recombination process can efficiently contribute to the formation of the H α and He II $\lambda4686$ emission lines.

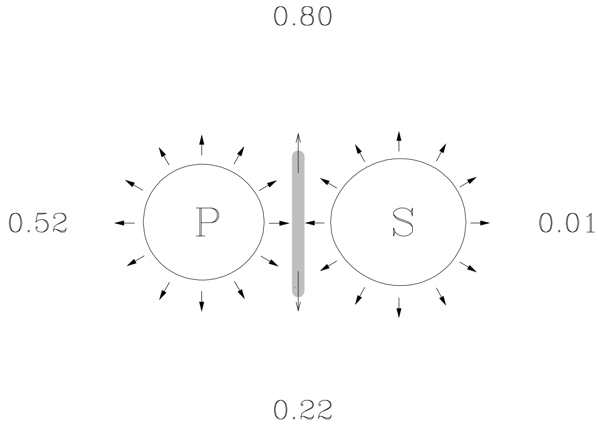

Fig. 11. Schematic view of the wind-wind interaction process occurring within the HD 152248 system. The shaded area represents the high density, emitting region. The P and S letters refer respectively to the primary and secondary components of the system. Conjunction and quadrature phases have been indicated. The adopted value for the separation between the two components is $53.1\mathrm{R}_\odot$, corresponding to $i = 67.2°$, and the shapes of the stars have been computed assuming mean radii $R_1 = 15.6\mathrm{R}_\odot$ and $R_2 = 17.1\mathrm{R}_\odot$ (Mayer et al. 2001) respectively.

A very simple model that can match most of the observations consists therefore in assuming the existence of a wind-wind interaction region located at mid-way from both stars and limited by two roughly planar hydrodynamic shocks. This high density region, where the He II $\lambda4686$ and H α emission components are assumed to be produced, would (partly) be occulted at conjunction phases ($\phi = 0.01$ and 0.52) which explains why the absorption is overwhelming near these phases. Similarly, this simple scenario also accounts for the phase-locked variations of the width of the emission component. Indeed, we expect from our model that the inner shock region would be almost perpendicular to the axis of the system, so that the distribution of the radial velocities of the particles escaping from the wind interaction region should be broader when our line of sight is aligned with the interaction zone (i.e. around $\phi = 0.22$ and 0.80). On the other hand, this velocity distribution should be narrower at conjunction phases when our line of sight is forming an angle of about $i \approx 70°$ with the interaction region. Near conjunction, we thus expect to observe a narrower emission line than around quadrature.

Part of the difference of the relative strengthening of the emission near quadrature phases might be explained by assuming that the emission process is depending of the separation D between the two stars following some power of 1/D. Indeed this distance is slightly larger at $\phi = 0.22$ than at $\phi = 0.80$. The difference between the two *absorption peaks* at conjunction phases might also result from a difference in the separation between the two stars since the phases $\phi = 0.0$ and $\phi = 0.5$ respectively coincide with the periastron and the apastron passage. The unequal depths of the primary and secondary eclipses might also account for part of this difference, as the continuum level is lower at primary eclipse and the dilution of the emission is thus weaker. We might expect that the forthcoming X-ray observations will help to address those questions and will further allow us to refine the wind-wind interaction model of the HD 152248 system.

9. Conclusion

We presented the results of an optical spectroscopic campaign on the HD 152248 O+O binary system. Based on a large set of medium and high resolution spectra which provides a very good phase coverage, we derived improved orbital parameters. Combining literature data with our observations, we detected the presence of an apsidal motion with a rate of about $3.4^\circ\,\mathrm{yr}^{-1}$. As this system is going to be observed with the XMM X-ray observatory, the new contemporaneous ephemerides we derived are of major importance to correctly interpret the X-ray observation of the HD 152248 binary.

We found that the previous classification of both components as supergiants is most probably erroneous and we provide a new classification as O7.5III(f) + O7III(f) for the system. This leads to a better agreement between the observed radii and masses of the components and the typical values for O7 - O7.5 giants. The masses we derived are however still significantly lower than the ones predicted by the evolutionary tracks.

Finally we demonstrated that the He II λ4686 and H α line profiles result from a blend of two absorption components, associated with the stars of the system, with a broader and more intense emission component. We further showed that their profile and intensity variations are consistent with a wind-wind collision process within the system, assuming that the He II λ4686 and H α emissions are produced within the interaction region through the recombination process.

The probable existence of a wind-wind interaction within the HD 152248 system makes this object an even more attractive target for XMM X-ray observations. The XMM pointings are scheduled to properly cover the orbital cycle and will further allow to investigate the different time scales of the wind interaction process. Detailed comparison of these data with recent theoretical hydrodynamical simulations (e.g. Stevens et al. 1992; Pittard 2000) will provide an important test for these models. It will further help to improve our understanding of the wind-wind collision process, and more widely of the winds of hot stars in general.

Acknowledgements. We wish to thank Dr. O. Stahl and Dr. A. Kaufer for their efficient help in adapting the FEROS reduction package to our data and the referee Dr. Stahl for his suggestions that improve our manuscript. We are grateful to Y. Nazé and Dr. J. Manfroid for their help in the reduction of the BME data. We thank Dr. J.-M. Vreux for many helpful comments and stimulating discussions. We are also grateful to Drs. P. Harmanec and P. Eenens for discussion about HD 152248 and for communicating their results prior to publication. We are greatly indebted to the Fonds National de la Recherche Scientifique (Belgium) for multiple supports. This research is also supported in part by contract P4/05 "Pôle d'Attraction Interuniversitaire" (SSTC-Belgium). Partial support through the PRODEX XMM-OM and INTEGRAL Projects is also gratefully acknowledged. The SIMBAD database has been consulted for the bibliography.

References

Bagnuolo, W.G.Jr., Gies, D.R., Riddle, R., & Penny, L.R. 1999, ApJ, 527, 353
Baume, G., Vázquez, R.A., & Feinstein, A. 1999, A&AS, 137, 233
Cardona-Núñez, O. 1978, PhD Thesis, University of Colorado, Boulder
Chlebowski, T., & Garmany, C.D. 1991, ApJ, 368, 241
Conti, P.S. 1973, ApJ, 179, 181
Conti, P.S., Leep, E.M., & Lorre, J.J 1977, ApJ, 214, 759
Corcoran, M.F. 1996, RevMexAA Conf., 5, 54
Eggleton, P.P. 1983, ApJ, 268, 368
Gayley, K.G. 2001, in Interacting Winds from Massive Stars, ASP Conf. Series, eds. A.F.J. Moffat, & N. St.-Louis, in press
Heck, A., Manfroid, J., & Mersch, G. 1985, A&AS, 59, 63
Hill, G., Crawford, D.L., & Barnes, J.V. 1974, AJ, 79, 1271
Hill, G.M., Moffat, A.F.J., St.-Louis, N., & Bartzakos, P. 2000, MNRAS, 318, 402
Howarth, I.D., & Prinja, R.K. 1989, ApJS, 69, 527
Howarth, I.D., Siebert, K.W., Hussain, G.A.J., & Prinja, R.K. 1997, MNRAS, 284, 265
Lafler, J., & Kinman, T.D. 1965, ApJS, 11, 216
Levato, H., & Morrell, N. 1983, ApL, 23, 183
Luna, H.G. 1988, A&AS, 74, 427
Mason, B.D., Gies, D.R., Hartkopf, W.I., et al. 1998, AJ, 115, 821
Mathys, G. 1988, A&AS, 76, 427
Mayer, P., Lorenz, R., & Drechsel, H. 1992, IBVS, 3765, 1
Mayer, P., Harmanec, P., Lorenz, R., et al. 2001, in The Influence of Binaries on Stellar Population Studies, ed. D. Vanbeveren, Kluwer Academic Publisher, in press
Meynet, G., & Maeder, A. 2000, A&A, 361, 101
Morrell, N.I., Walborn, N.R., & Fitzpatrick, E.L. 1991, PASP, 103, 341
Nussbaumer, H. 1971, ApJ, 170, 93
Penny, L.R., Gies, D.R., & Bagnuolo, W.G.Jr. 1996, ApJ, 460, 906
Penny, L.R., Gies, D.R., & Bagnuolo, W.G.Jr. 1999, ApJ, 518, 450
Pittard, J.M. 2000, PhD Thesis, University of Birmingham (UK)
Pittard, J.M., & Stevens, I.R. 1997, MNRAS, 292, 298
Raboud, D., Cramer, N., & Bernasconi, P.A. 1997, A&A, 325, 167
Rauw, G., Vreux, J.-M., & Bohannan, B. 1999, ApJ, 517, 416
Rauw, G., Sana, H., Gosset, E., et al. 2000, A&A, 360, 1003
Rauw, G., Sana, H., Vreux, J.-M., Gosset, E., & Stevens, I.R. 2001, in Interacting Winds from Massive Stars, ASP Conf. Series, eds. A.F.J. Moffat, & N. St.-Louis, in press
Sana, H., Rauw, G., Gosset, E., & Vreux, J.-M. 2001, in Interacting Winds from Massive Stars, ASP Conf. Series, eds. A.F.J. Moffat, & N. St.-Louis, in press
Schaller, G., Schaerer, D., Meynet, G., & Maeder, A. 1992, A&AS, 96, 269

Stevens, I.R., Blondin, J.M., & Pollock, A.M.T. 1992, ApJ, 386, 265
Stickland, D.J., Lloyd, C., Penny, L.R., Gies, D.R., & Bagnuolo, W.G.Jr. 1996, Observatory, 116, 226
Struve, O. 1937, ApJ, 85, 41
Struve, O. 1944, ApJ, 100, 189
Thaller, M.L. 1997, ApJ, 487, 380
Underhill, A.B. 1994, ApJ, 420, 869
Vink, J.S., de Koter, A., & Lamers, H.J.G.L.M. 2000, A&A, 362, 295
Walborn, N.R. 1972, AJ, 77, 312
Walder, R. 1998, Ap&SS, 260, 243
Wolfe, R.H.Jr., Horak, H.G., & Storer, N.W. 1967. in Modern Astrophysics, ed. M. Hack, Gordon & Breach, New York, 251